Low friction in bcc metals via grain boundary sliding

Adam R. Hinkle, John F. Curry, Hojun Lim, Brendan L. Nation, Morgan R. Jones, John Wellington-Johnson, Ping Lu, Nicolas Argibay,* and Michael Chandross†

Material, Physical, and Chemical Sciences Center, Sandia National Laboratories, Albuquerque, New Mexico 87123, USA

(Received 25 February 2020; revised manuscript received 1 May 2020; accepted 20 May 2020; published 8 June 2020)

Low friction is demonstrated with pure polycrystalline tantalum sliding contacts in both molecular dynamics simulations and ultrahigh vacuum experiments. This phenomenon is shown to be correlated with deformation occurring primarily through grain boundary sliding and can be explained using a recently developed predictive model for the shear strength of metals. Specifically, low friction is associated with grain sizes at the interface being smaller than a critical, material-dependent value, where a crossover from dislocation mediated plasticity to grain-boundary sliding occurs. Low friction is therefore associated with inverse Hall-Petch behavior and softening of the interface. Direct quantitative comparisons between experiments and atomistic calculations are used to illustrate the accuracy of the predictions.

DOI: 10.1103/PhysRevMaterials.4.063602

I. INTRODUCTION

Sliding friction between pure, coarse-grained metals (e.g., Au, Ag, Cu, and Fe) is typically high [1–4], with friction coefficients $\mu > 1$. High friction is particularly common when the contacting surfaces are devoid of oxides that, depending on the metal, can readily form and reform in the presence of oxygen. Oxide films can, at least partially, inhibit direct metal-on-metal contact, mitigating the strong adhesion associated with clean metallic interfaces. Self-mated pure metal interfaces are effectively indistinguishable from bulk metal, although shear-induced deformation can lead to finer-grained microstructures near sliding interfaces. These ultrananocrystalline microstructures result in localized mechanical strengths that can differ significantly from the bulk flow strength. Low friction ($\mu < 0.5$) in metal contacts has been reported in experiments with some pure metals [2,3], and has more recently been associated with the microstructural changes generated near the sliding interface [5] (and references therein). Specifically, an ultrananocrystalline layer approximately 100 nm thick with grain sizes ∼10 nm—a microstructural feature that is often substantially different from the bulk material, as mentioned above—has been observed at the interface in metal contacts exhibiting low friction. A model was recently developed in [5] for fcc metals that describes the low and high friction regimes in self-mated metal contacts, and links them to the near-surface microstructural evolution as a function of applied stress, temperature, and time in contact during sliding. The presence of an ultrananocrystalline surface layer was hypothesized to be directly associated with low friction by acting as an interface with reduced shear strength. The ratio of this interfacial shear strength with the bulk hardness of the material (a property that is not changed through tribological contact) gives an approximation of the friction coefficient, as described by Bowden and Tabor [6]. The ultrananocrystalline nature of this layer reduces shear strength by promoting grain boundary sliding (GBS) [7–15] as the principal deformation mechanism. Conversely, when the surface microstructure consists of coarser grains, the dominant mechanism is dislocation mediated plasticity (DMP), and friction is high. GBS has been proposed as the mechanism behind inverse Hall-Petch behavior in metals [16–18] and has been previously discussed in the context of low friction and wear [5,19–23].

These recent insights have advanced the understanding of the fundamental processes responsible for the atomic-scale mechanisms of friction in fcc metals, and have motivated similar investigations into the friction regimes of bcc metals. The question of whether, like fcc metals, a low-friction regime exists for bcc metals has received little attention. Plasticity in polycrystalline metals is generally ascribed to the nucleation and motion of dislocations along well-defined slip planes and directions. The different geometries of fcc and bcc lattices lead to differences in the types of dislocation activity, the stresses required for their activation and motion, and the dependence of the activity on temperature and the rate of external loading. While partial dislocations separated by stacking faults are the dominant carriers of plasticity in fcc metals, in bcc metals screw dislocations, which cannot dissociate into partial dislocations, are generally found at low temperatures. These differences result not only in bcc metals tending to be much less ductile than their fcc counterparts, but also strong dependencies of their mechanical properties (e.g., yield strength and hardness) on the applied strain rate and temperature [24–29].

These differences might suggest that the mechanisms of friction in bcc metals could be substantially different from those of fcc metals. There is evidence, however, in bcc Mo that, like fcc metals, grain size greatly influences how plasticity is mediated, and that below approximately 30 nm in grain size the dislocation density drops to nearly zero [30].

*Corresponding author: nargiba@sandia.gov
†Corresponding author: mechand@sandia.gov

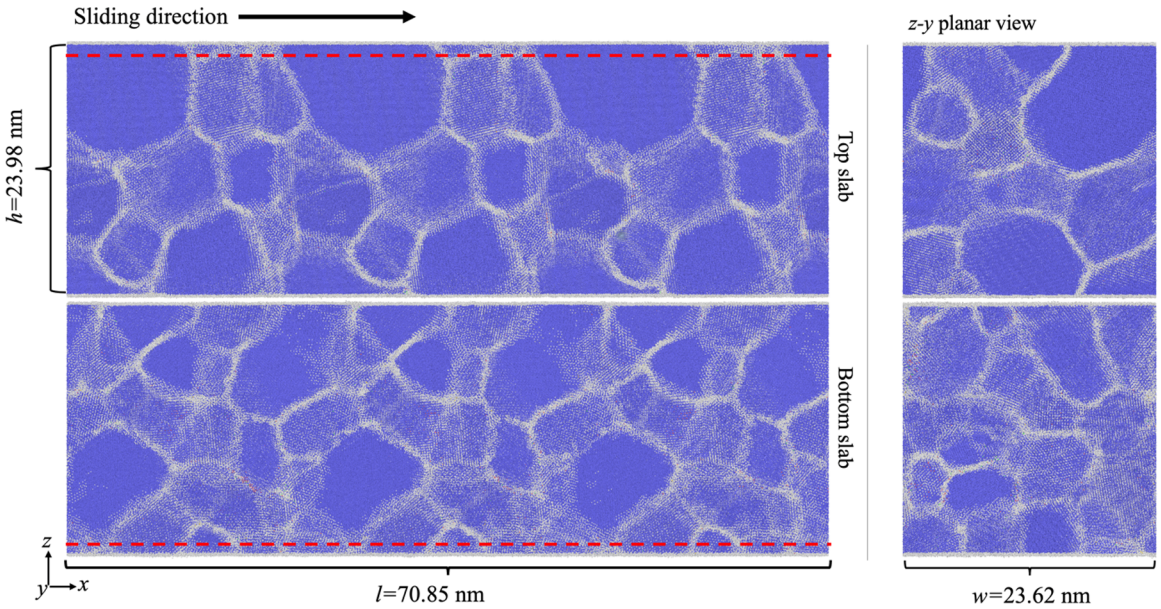

FIG. 1. Molecular dynamics setup of slabs of bcc polycrystalline Ta shown with front (left) and side (right) views. A constant velocity is prescribed to a thin layer of atoms at the upper surface (above red dashes) of the top slab which induces sliding under a constant applied normal stress. A thin layer of atoms at the bottom (below red dashes) is held fixed at zero force and velocity. The bcc grains (blue) with random orientations of the as-prepared microstructure before sliding are approximately 5–10 nm in diameter. Uncoordinated atoms (gray) primarily indicate grain boundaries.

The possibility then arises that the generation of an ultra-nanocrystalline surface layer in a sliding bcc contact will lead to deformation through GBS and concomitant low friction. Recent molecular dynamics (MD) simulations of bcc Ta have also suggested that GBS is the dominant mechanism accommodating deformation in grains ∼10 nm, and that inverse Hall-Petch behavior occurs [31]. Chandross and Argibay have recently developed a theory with no arbitrary or adjustable parameters that describes GBS in terms of amorphization, and relates it to the grain size dependent shear strength of the material [32]. While the demonstration of low friction via GBS could be interpreted as room-temperature superplasticity, there is a distinction from previous work. For example, Raj and Ashby [12] explain superplasticity in the context of thermally activated processes, while the amorphization theory (which also accounts for thermal activation) relies primarily on stress-driven amorphization to accommodate deformation [32]. It is also important to note that the amorphization theory is not exclusively applicable to planar interfaces; the deformation of contacts of any geometry can occur by amorphization. Such a process energetically favors shear along a thin plane of atoms that transects the metal-metal junction regardless of the initial shape or roughness. While these factors affect the contact area and degree of interlocking of asperities, the process of amorphization can proceed across that junction regardless of the initial conditions.

We present the results of atomistic simulations and experiments that were used to investigate the friction behavior of bcc metals, using Ta as an exemplar. We show that a low friction regime exists, and that the shear strength can be explained by models that agree well with both our results and those from the available literature.

II. MOLECULAR DYNAMICS SIMULATIONS

A. Setup

We study the friction behavior of Ta using molecular dynamics simulations with an EAM potential [33] and the LAMMPS simulation code [34]. Polycrystalline slabs of Ta were created using the phase-field approach described in detail in [35], where grains are generated according to the energies that drive microstructural evolution. Atomistic structures were generated by filling the regions identified as grains with atoms on a bcc lattice, with random rotations for each grain. The energy was minimized and pressure reduced to zero before annealing at 500 K, followed by cooling to 300 K over 1 ns. Two independently created and relaxed polycrystalline slabs, each with an as-prepared average grain size of approximately 5–10 nm, were then brought into contact as shown in Fig. 1. The total system consists of approximately 4 million atoms, with each slab having initial dimensions 71 nm × 24 nm × 24 nm in the x, y, and z directions, respectively.

To determine shear strength, a constant velocity v_x was applied in the x direction to all atoms in a 1-nm-thick slice of the upper end of the top slab. A normal stress σ in the negative z direction was also imposed on these atoms. A similar slice at the opposite end of the bottom slab had zero velocities and forces imposed. Integration was performed using a time step of 1 fs with a Langevin thermostat at 300 K that only included degrees of freedom in the y direction (i.e., perpendicular to the applied normal force in z and velocity in x). All systems underwent total simulation times of approximately 40 ns.

A range of normal stresses and velocities were studied, $\sigma = 0.1$, 0.4, 0.6, 0.8, and 1.0 GPa, and $v_x = 0.5$, 1.0, 1.5, 2.0, and 5.0 m/s. The normal stress was calculated from the

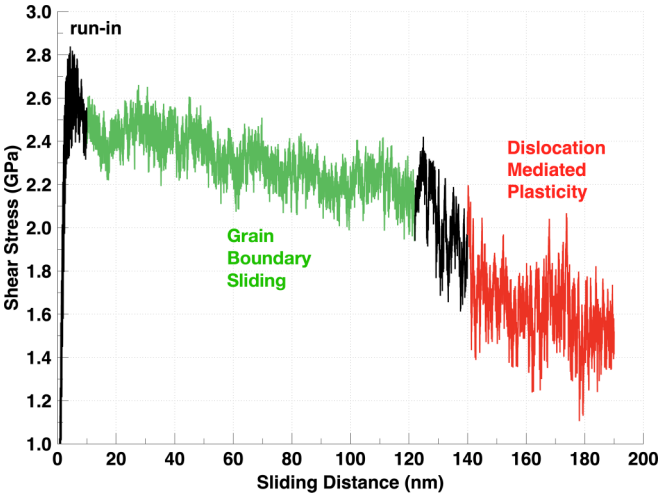

FIG. 2. Shear stress as a function of the displacement of the thin top layer in the MD simulations of bcc polycrystalline Ta, shown for a velocity $v_x = 5\,\mathrm{m/s}$ with a normal load of 600 MPa. Two distinct regimes of sliding are observed after run-in: In the early stages of sliding, nearly all grain movement is confined to motion along grain boundaries (grain boundary sliding). As grain growth proceeds, dislocation activity increases, and a transition to a lower shear stress occurs.

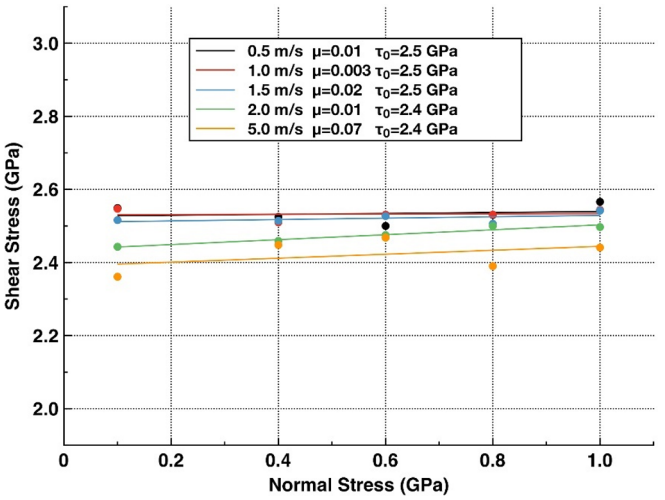

FIG. 3. Friction coefficient μ and shear stress τ from MD simulations of bcc polycrystalline Ta at different applied sliding velocities and normal stresses. A least-squares fit to $\tau = \tau_0 + \mu\sigma$ is shown for each velocity.

total normal force divided by the transverse area of the slabs. As this area does not change throughout the simulations, we will hereafter discuss results in the context of applied normal stresses. Similarly, the total force in the x direction on the thin top slice was averaged in time every ten time steps to calculate the shear stress. These boxcar average values of shear stress are shown in Fig. 2 as a function of the displacement in the direction of sliding. A distinct change in shear stress can be seen, and we show below that this is correlated with a transition from GBS to DMP. It is interesting to note that, while we generally associate GBS with lower friction, Fig. 2 shows that the shear stress in the DMP regime was actually lower than that in the GBS regime. As is verified below, this indicates that the initial grain size was near the peak of the Hall-Petch curve, and demonstrates the reduction in strength with increasing grain size expected in the Hall-Petch (DMP) regime.

B. Friction and shear strength

Friction coefficients can be determined from simulations using the empirical equation [6,36]

$$\tau = \tau_0 + \mu\sigma, \tag{1}$$

where the interface shear strength τ is linearly related to the normal stress σ by the friction coefficient $\boldsymbol{\mu}$, i.e., the contact area-dependent component, and a contact area-independent component τ_0 that can be determined at zero applied normal load [36]. To calculate the magnitude of τ, shown in Fig. 3, we averaged over approximately the first 10 ps of sliding. This period, while brief, encompasses the time where sliding was nearly exclusively a result of GBS along the initial slab-to-slab interface, as identified through velocity profiles. The velocity profiles were constructed from averages of the x component of the atomic velocities in bins of approximately 1 nm thickness along the z direction. When GBS is the dominant mechanism of deformation, this profile shows a sharp interface between the top and bottom slabs, whereas the profile shows a less well-defined transition after grain growth leads to the dominance of DMP. An example is shown in Fig. 4, where the GBS regime can be identified in Fig. 4(a) and the DMP regime in Fig. 4(b).

The calculated values of τ and σ were used in Eq. (1) to fit for values for μ and τ_0, as shown in Fig. 3. Very low friction coefficients (close to zero) were found for all velocities, and both μ and τ_0 show only a weak dependence on v_x. Because of the spread in τ and σ as a function of time, error bars on the data in Fig. 3 would be large compared to the mean, and thus we consider these results to be essentially independent of velocity in this range. A vanishingly small friction coefficient implies that interface shear strength is insensitive to normal stress, and this can be attributed to the contact area being load-independent for these slab-on-slab simulations. It is important to recognize, however, that there are other effects of changing applied normal stress. For example, applied normal stress also plays a role in driving grain growth kinetics via grain boundary shear coupling [37], which can significantly impact interface shear strength evolution. This behavior can be seen in similar slab-on-slab simulations with pure Ag and Cu-Ag [Fig. 7(A) in [5]], where there was a measurable difference in friction coefficient between the pure metal and alloy. In those simulations, the microstructures were initially identical, but the alloy exhibited quantitatively less grain growth and a lower friction coefficient during an equivalent period of sliding shear. However, friction coefficients were similarly small ($\mu \sim 0.05$) and representative of a relatively weak coupling to normal load.

C. Microstructural evolution

To probe the atomistic mechanisms of shear strength we examined the microstructural evolution of the slabs during

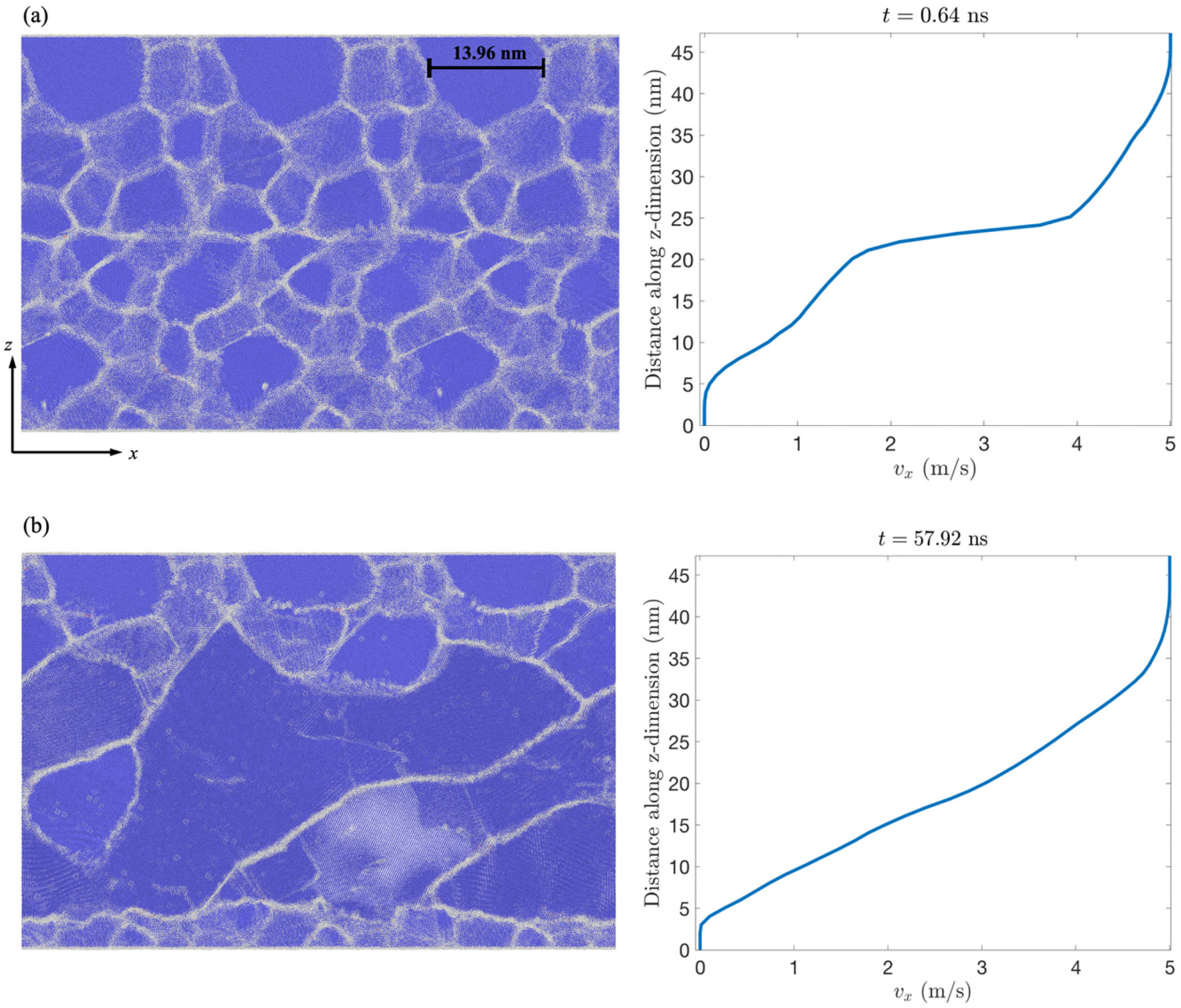

FIG. 4. Snapshots of MD simulations showing an example of the evolution of bcc polycrystalline Ta (left) shown alongside the corresponding profile of the x component of the atomic velocities (right) averaged along the z dimension. The bottom was held fixed while a velocity of 5 m/s in the x direction and a normal stress of 1.0 GPa were applied to the top. (a) Initially, grain sizes were close to the as-prepared system and sliding primarily occurred along the original interface of the slabs, as can be clearly seen in the abrupt change in the velocity profile between $z = 20-25$ nm. (b) Evidence of the original interface has disappeared as sliding became nearly homogenous throughout the bulk. Significant grain growth occurred as the system transitioned to a steady state where a nearly linear velocity profile emerged, similar to Couette flow observed in a viscous fluid.

sliding. Examples of these microstructures are shown in Fig. 4, where we show snapshots of the slabs with their respective velocity profiles.

Early in the simulations, grain sizes remain relatively unchanged from their initial size of ∼5–10 nm, and the original interface between the contacting slabs (near the middle) is still detectable via common neighbor analysis. This interface is where most of the shear deformation occurs initially, as reflected in the velocity profiles. As sliding continues, this interface rapidly disappears and is accompanied by an evolution of the microstructure toward larger grains with a nearly linear velocity profile, similar to that of Couette flow in viscous liquids [38]. Dislocation analysis of the grains using OVITO [39] revealed little dislocation activity in the small grains during the early period of sliding in the GBS regime. For example, 123 segments of $\frac{1}{2}\langle 111\rangle$ edge and screw dislocations, the primary carriers of plasticity in bcc crystals [30,40], are found forming a total length of 409.3 nm during initial sliding. Eventually grains increase to the sizes shown in Fig. 4(b) (some reaching approximately 50 nm in the direction of shear), and 397 segments are found with a total length of 1906.6 nm. In bcc Mo, dislocation activity has been experimentally shown to be strongly affected by grain size, with predominantly screw dislocations active above about 200 nm, and edge and mixed dislocations from about 50 to 150 nm [30]. Below 30 nm, grain boundary mediated processes are expected to become the dominant mechanism for plasticity [30]. As for fcc metals [5], we expect the grain size delineating the crossover between

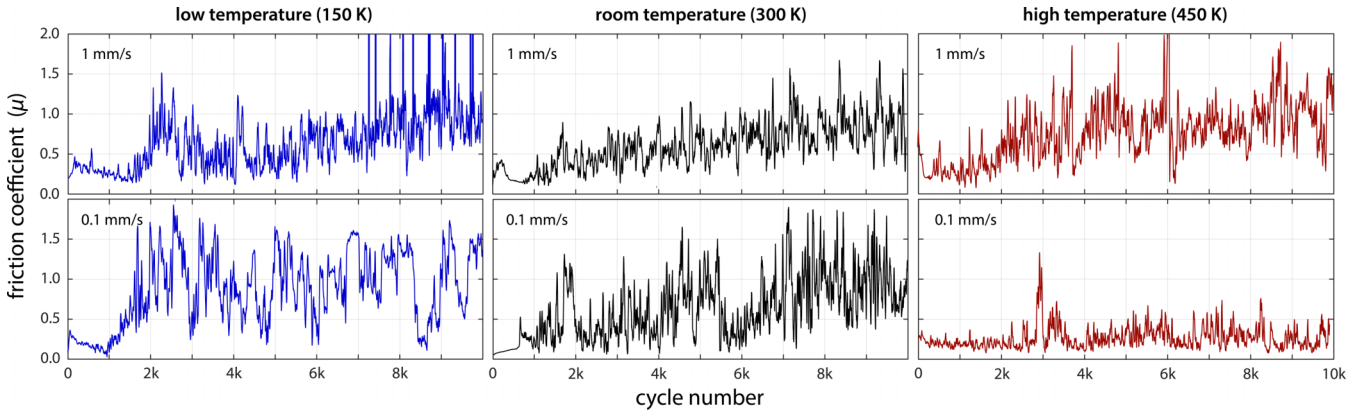

FIG. 5. Measurements of the friction coefficient from crossed-cylinder bidirectional reciprocating sliding experiments of Ta (3.175-mm-diameter rods) performed in UHV ($<1 \times 10^{-8}$ Torr) under 10 mN load.

GBS and DMP to be material dependent, and for Ta the results here indicate a critical grain size between 10 and 50 nm.

III. Ta FRICTION EXPERIMENTS IN UHV

Sliding experiments were performed with bcc polycrystalline Ta using high-purity 3.175-mm-diameter crossed cylinders in a custom-built ultrahigh vacuum (UHV) tribometer, including a cryostat and heating elements, that enables variation of contact temperature. The tribometer is similar in construction to those described in [41,42] and relies on capacitance probes to measure displacements of a calibrated two-axis flexural cantilever that was designed to generate linear vertical and horizontal deflections proportional to surface normal and friction forces, respectively.

Friction tests were performed with a 10-mN applied normal load, two different sliding speeds of 1 and 0.1 mm/s, chamber pressures $<1 \times 10^{-8}$ Torr, and temperatures of 150, 300, and 450 K. Reported temperatures were measured using a *K*-type thermocouple mechanically attached to one of the two Ta cylinders, and the system was cooled or heated while the cylinders were in contact to ensure thermal equilibrium. Samples were fixtured using Macor parts, which have relatively low thermal conductivity, and sliding was not initiated until there was negligible observed drift in displacement (measured as a change in contact force) due to temperature equilibration of the system. As shown in Fig. 5, all test conditions initially showed low friction ($\mu < 0.5$). However, except for the high-temperature/low sliding speed case, all evolved to high friction ($\mu > 1$) in the first 1000–2000 sliding cycles. It is likely that this run-in period is associated with the removal of the native oxide from both cylinder surfaces that, as mentioned in the Introduction, can inhibit metal-to-metal contact and produce temporarily low friction even in UHV environments. It is not surprising that the run-in period takes over 1000 cycles to expose bare metal on both surfaces, given the low applied contact force of 10 mN. These data indicate there was a negligible effect of temperature on the run-in process and no significant qualitative difference in the evolution to high friction coefficients. At the slowest speed and highest temperature, however, there were notable differences, including the evolution of low friction that was persistent for the entire 10 000 cycle experiment.

An important distinction of this work is the apparent antithermal friction behavior of bcc Ta. In fcc metals, the suppression of the thermally driven grain growth at lower temperatures leads to the dominance of shear-induced grain refinement, thus promoting lower friction through GBS [5]. In contrast, higher temperatures in fcc metals leads to grain growth and increased dislocation activity [43], with concomitant higher friction [23]. For high melting temperature refractory metals like Ta, a small increase of about 150 K above room temperature can activate a transition from brittle to ductile behavior [26]. This increase maintains a relatively low homologous temperature ($\sim$0.14), and only a small increase in grain growth rates even for nanocrystalline metals [43,44]. In contrast, there will be a significant strength reduction associated with the thermally activated motion of screw dislocations [26]. A decrease in sliding speed (i.e., strain rate) was used to further promote the brittle to ductile transition [26]. The combination of increased temperature and decreased strain rate results in a dramatic reduction in shear strength and friction coefficient. The results of the variable temperature and sliding speed UHV friction experiments, summarized in Fig. 5, can be explained in this context, as only the lowest sliding speed (0.1 mm/s) and highest temperature (450 K) resulted in a low friction coefficient ($\mu \sim 0.4$).

The microstructures of the Ta samples after sliding were investigated by scanning transmission electron microscopy (STEM). Samples were produced with the focused ion beam (FIB) method. STEM utilized a probe-corrected FEI Titan^{TM} G2 80-200 microscope operated at 200 kV and recorded the images with the high-angle annular dark-field (HAADF) detector with a collection range of 60–160 mrad. The two representative examples shown in Fig. 6 for low and high friction wear tracks show substantial differences in the surface and subsurface microstructure. The low friction case shows the formation of a surface layer of highly refined grains, in contrast to the visibly coarser grains in the high friction case. These observations are in agreement with those for fcc metals, where low friction has been correlated with the formation of a thin ultrananocrystalline layer at the sliding surface; see Ref. [5] and references therein. As discussed above, these results differ from previous experimental reports of temperature-dependent friction regimes with fcc metals [5,23], where lower friction was associated with lower

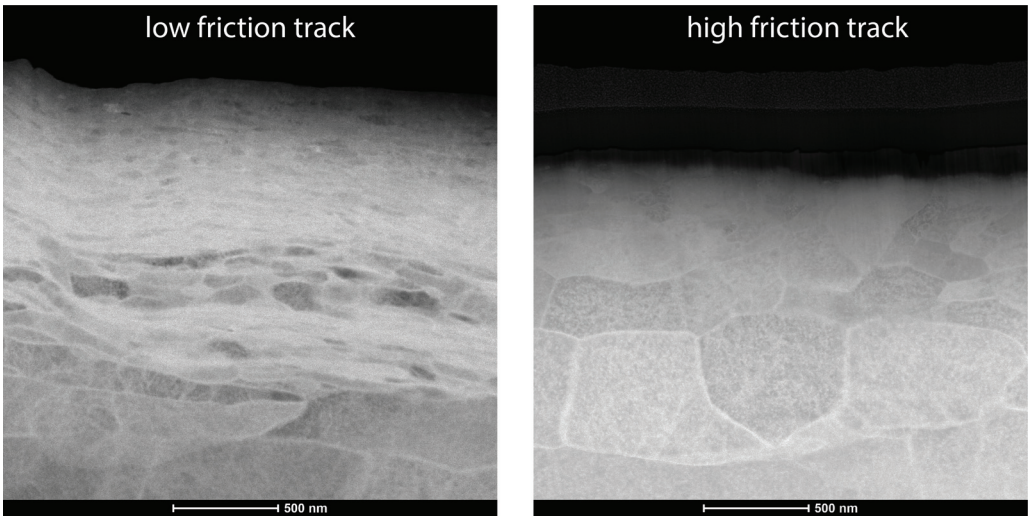

FIG. 6. STEM images of bcc polycrystalline Ta wear track after sliding friction experiments. The highly refined grain structure (left) is representative of the wear track at 450 K and 0.1 mm/s where low friction ($\mu \sim 0.4$) was achieved, contrasting with the coarse-grained microstructure (right, experiments at 300 K and 1.0 mm/s) representative of wear tracks with high friction ($\mu \sim 1.4$; see Fig. 5).

temperature. For fcc metals, lower friction at lower temperatures was attributed to the slowing of grain growth kinetics, enabling grain refinement to prevail, while a temperature-induced transition from brittle to ductile behavior is an additional factor for bcc metals.

It is important to note that very small grains, especially those in the ultrananocrystalline regime, are not thermodynamically stable, and grain growth is essentially unavoidable during the time between the friction experiments and the STEM analysis. For this reason, the grain sizes seen in Fig. 6 form an upper bound of the sizes during dynamic sliding. This is an important point to make for the discussion of the grain size dependent shear strength of metals.

IV. SHEAR STRENGTH OF NANOCRYSTALLINE Ta

To understand the relationship between friction coefficient and grain size, it is helpful to view these results in the context of the grain-size dependent strength of metals. Figure 8 shows a plot of predicted and measured grain size-dependent shear strengths for Ta, including the results of our simulations, MD simulations from [31], experimental data for Ta from the review of Hall-Petch behavior in [45], and a fit to the Hall-Petch relationship, $\sigma_Y = \sigma_0 + \frac{k}{\sqrt{d}}$, where σ_Y is the measured uniaxial yield stress, d is the mean grain size, and σ_0 and k are constants. Note that in Fig. 7 we have converted yield strengths to shear strengths, τ_Y, using the von Mises stress criterion, $\tau_Y = \frac{\sigma_Y}{\sqrt{3}}$. Also shown in Fig. 7 are the predicted shear strengths from a recently proposed predictive model of GBS [32] that accurately predicts the data (see below).

From Fig. 7 we estimate a critical grain size of $d_c = 30 - 40$ nm as the crossover point between the grain boundary sliding and dislocation mediated plasticity regimes. Note the similarity to the grain size in Mo where dislocation activity ceases [30], and agreement with the range of grain sizes where the transition was estimated from Fig. 4. While data for more bcc metals are needed to support the general validity of this conclusion, these data indicate that the critical grain sizes for bcc metals are about two to three times those reported for fcc metals, where $d_c = 10 - 20$ nm [5]. At grain sizes larger than d_c the shear strength follows typical Hall-Petch behavior and is well described by models of dislocation mediated plasticity in bcc metals [26,30,46].

The GBS model prediction shown in Fig. 7 (red line) relates shear strength to the energy required to transform crystalline material into an amorphous phase [32], i.e., to continuously or dynamically (re)form an amorphous layer along

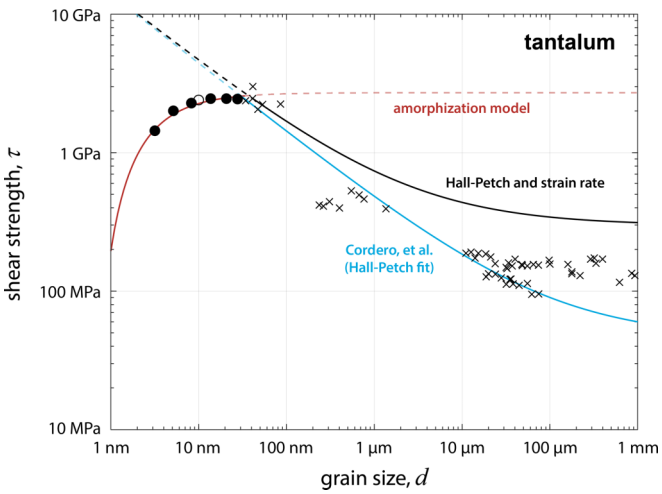

FIG. 7. The shear strength of bcc Ta as a function of grain size as compiled from experiments in the literature (black x) [45] and MD simulations from this work (open circle) and Tang *et al.* (solid black circles) [31]. The amorphization theory of GBS [32] as parametrized for Ta (red curve) is shown intersecting a fit of the Hall-Petch equation (blue) to the experimental data for Ta in [45], along with a Hall-Petch fit (black curve) from a crystal plasticity model that illustrates the variability due to strain rate. The intersections of these models (curves) occur at approximately $d_c = 30 - 40$ nm, defining the critical grain size that marks a transition in deformation mechanism from GBS to DMP.

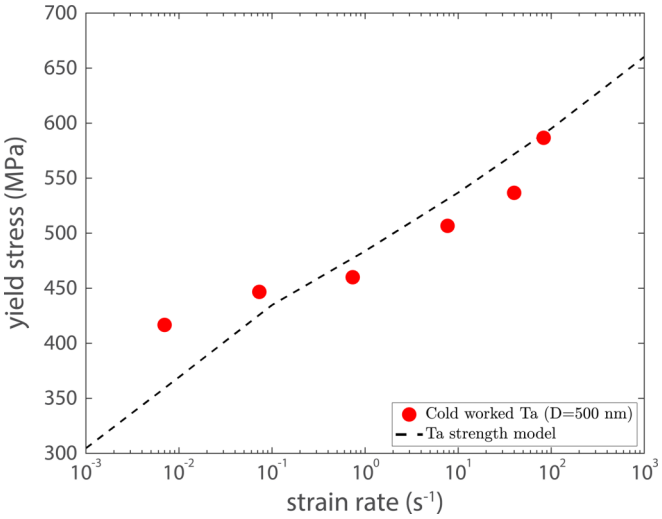

FIG. 8. Yield stresses taken as 1/3 the measured hardness values (red dots) from the data in Fig. S1 in the Supplemental Material [49]. The dashed lines show the theoretical yield strengths as calculated from the kink-pair theory described in [26,46].

the shearing interface. This prediction builds on previous work describing GBS as viscous flow at grain boundaries and uses no arbitrary or fitting parameters, relying exclusively on material properties and physically meaningful input parameters including grain size and temperature. The expression for the shear strength describing the simulation data can be written as

$$\tau = L\frac{\rho_L}{M}\left(1 - \frac{T}{T_m}\right) f_g. \tag{2}$$

A detailed discussion of the physical constants in Eq. (2) can be found in [32], but are briefly listed in Table I with their values. Included in Eq. (2) is the volume fraction of crystalline material in grains, $f_g = (\frac{d-\delta}{d})^3$, where δ is the grain boundary width, estimated as twice an atomic diameter.

Equation (2) is derived from an Eyring-type model [48] with the free energy change of the material being the difference between crystalline and amorphous phases that was shown to be related to the heat of fusion [32]. For grains below d_c, the shear strength increases with grain size, until the shear strength from amorphization exceeds that required for dislocation activity (represented by the best fit of the Hall-Petch relationship to a wide range of data from [45]). In addition to the prediction from the amorphization model (red curve) in Fig. 7, we show the shear strength calculated from our MD simulations from Sec. II, as well as independent MD simulations of the tensile strength of Ta from [31]. Excellent agreement is found between the GBS model predictions and simulation data, and this strongly suggests that GBS via dynamic amorphization is indeed the dominant mechanism accommodating the imposed shear. The curves in Fig. 7 also allow for an estimate of the dynamic grain size during shear, by using the relationship that friction coefficients can be approximated as the ratio of near-surface shear strength to bulk hardness [6,36]. With a hardness of ∼1.5 GPa, determined by scratch testing (see the Supplemental Material [49], including Refs. [50–60]), the friction coefficient of 0.4 found in the low friction case implies an interfacial shear strength of ∼600 MPa. From the amorphization and Hall-Petch curves in Fig. 7, this strength implies a grain size of either ∼1–2 nm (near-amorphous) or ∼0.6–2.0 μm. As the TEM analysis of Fig. 6 gives, at best, an upper bound on the grain size present during sliding, the 0.6–2.0 μm case can be ruled out, implying that dynamic grain sizes during shear are extremely small, and approach the amorphous limit, as described by the GBS theory.

TABLE I. The physical constants used for calculations of shear strength based on the GBS model in [32] and their values for Ta; the value of ρ_L was taken from [47].

T	Temperature	300 K
T_m	Melting temperature	3290 K
δ	Grain boundary width	0.5 nm
L	(Latent) heat of fusion	36 kJ/mol
M	Molar mass	0.181 kg/mol
ρ_L	Liquid density at T_m	15 010 kg/m^3

For grains larger than d_c, Hall-Petch behavior is observed and can be accounted for using dislocation mediated plasticity models (see below), implying that GBS is no longer the dominant mechanism once grains are large enough to support dislocation nucleation and movement. The strength of Ta in the dislocation plasticity regime, i.e., when grain sizes are above approximately 30 nm (for strain rates below ∼ 10^4 s^{-1}), can be described by the Hall-Petch equation and dislocation kink-pair theory [24,26,27,61] as follows:

$$\sigma_Y = \bar{\sigma} + \sigma^*(T, \dot{\gamma}). \tag{3}$$

Here, $\bar{\sigma}$ is the athermal obstacle strength from dislocation interactions and $\sigma^*(T, \dot{\gamma})$ is the temperature and strain rate, $\dot{\gamma}$, dependent lattice resistance. Based on the dislocation kink-pair theory $\sigma^*(T, \dot{\gamma})$ can be determined from

$$\sigma^*(T, \dot{\gamma}) = \bar{M} \min(\tau^*_{EI}(T, \dot{\gamma}), \tau^*_{LT}(T, \dot{\gamma})), \tag{4}$$

where $\bar{M}$ is the average Taylor factor that represents the ratio between the macroscopic stress and the resolved shear stress, and $\tau^*_{EI}(T, \dot{\gamma})$ and $\tau^*_{LT}(T, \dot{\gamma})$ are the stresses calculated from the elastic interaction and line tension models, respectively. These two stresses describe the flow behavior of bcc metals in different temperature and strain rate regimes; a detailed presentation is provided in [26,46]. Using the criterion that the hardness of a cold-worked metal is approximately three times its yield stress, yield stresses (and thus shear strengths) for Ta can be obtained from the data in Fig. S1 in the Supplemental Material [49] as a function of applied strain rate. Comparison is made to the theoretical strengths as calculated from the kink-pair theory in Fig. 8. We note that the $\bar{\sigma}$ value of 164 MPa, calculated from a fit to the model, accounts for the athermal part of the stress. Figure 8 shows that the experimentally measured shear strengths in the dislocation mediated plasticity regime are reasonably captured by dislocation kink-pair theory. In particular, the effect of strain rate on the Hall-Petch shear strength is apparent.

V. SUMMARY AND CONCLUSIONS

We have presented evidence of low friction in bcc metal sliding contacts from atomistic simulations and experiments. These results present compelling evidence that GBS is the dominant deformation mechanism in polycrystalline Ta when grain sizes are less than approximately 30 nm. We have shown predictions from a recently proposed model that considers dynamic amorphization of crystalline material as the mechanism behind GBS, showing good agreement with available experimental and simulated data. Conversely, for grain sizes larger than 30–40 nm, dislocation activity is the dominant plasticity accommodation mechanism, and the strain rate and temperature-dependent shear strengths are well described by a recently proposed crystal plasticity model.

Although our present results are based on investigations of shear strength and friction coefficient in Ta, the applicability of the GBS shear strength models to a wide range of bcc and fcc metals remains a possibility and merits further attention. The focus of this work was a determination of the role of inverse Hall-Petch behavior on shear strength of sliding contacts, a mechanism that manifests in many nanocrystalline metals at the sliding interface where grains can become highly refined. This work strongly suggests that the GBS regime is associated with the dynamic amorphization of crystalline material at sliding interfaces. For a given metal, the energy associated with amorphization can be readily calculated using materials properties, defining a maximum shear strength and the observed decreasing shear strength with decreasing grain size below a critical size d_c. The critical grain size marking the transition from GBS to DMP depends on the metal composition, and in the case of bcc Ta appears to be about two to three times that of fcc metals.

ACKNOWLEDGMENTS

Sandia National Laboratories is a multimission laboratory managed and operated by National Technology and Engineering Solutions of Sandia, LLC, a wholly owned subsidiary of Honeywell International, Inc., for the US Department of Energy's National Nuclear Security Administration under Contract No. DE-NA0003525. This work was funded by the Laboratory Directed Research and Development (LDRD) program. Any subjective views or opinions that might be expressed in the paper do not necessarily represent the views of the US Department of Energy or the United States Government.

[1] R. Holm, *Electric Contacts: Theory and Application*, 4th Ed. (Springer-Verlag, New York, 1967).
[2] Y. Tamai, J. Appl. Phys. **32**, 1437 (1961).
[3] T. F. Bowden and T. P. Hughes, Nature (London) **142**, 1039 (1938).
[4] J. R. Whitehead, Proc. R. Soc. London, Ser. A **201**, 109 (1950).
[5] N. Argibay, M. Chandross, S. Cheng, and J. R. Michael, J. Mater. Sci. **52**, 2780 (2017).
[6] F. P. Bowden and D. Tabor, Nature (London) **150**, 197 (1942).
[7] A. Ball and M. M. Hutchison, Met. Sci. J. **3**, 1 (1969).
[8] R. C. Gifkins, Metall. Trans. A **7**, 1225 (1976).
[9] T. G. Langdon, Acta Metall. Mater. **42**, 2437 (1994).
[10] T. G. Langdon, Philos. Mag. **22**, 689 (1970).
[11] T. G. Nieh, J. Wadsworth, and O. D. Sherby, *Superplasticity in Metals and Ceramics* (Cambridge University Press, Cambridge, UK, 1997).
[12] R. Raj and M. Ashby, Metall. Mater. Trans. B **2**, 1113 (1971).
[13] O. D. Sherby and J. Wadsworth, Prog. Mater. Sci. **33**, 169 (1989).
[14] R. N. Stevens, Philos. Mag. **23**, 265 (1971).
[15] T. G. Langdon, J. Mater. Sci. **41**, 597 (2006).
[16] M. A. Meyers, A. Mishra, and D. J. Benson, Prog. Mater. Sci. **51**, 427 (2006).
[17] A. H. Chokshi, A. Rosen, J. Karch, and H. Gleiter, Scr. Metall. **23**, 1679 (1989).
[18] G. E. Fougere, J. R. Weertman, R. W. Siegel, and S. Kim, Scr. Metall. Mater. **26**, 1879 (1992).
[19] D. Shakhvorostov, B. Gleising, R. Büscher, W. Dudzinski, A. Fischer, and M. Scherge, Wear **263**, 1259 (2007).
[20] D. Shakhvorostov, K. Pöhlmann, and M. Scherge, Wear **260**, 433 (2006).
[21] S. V. Prasad, C. C. Battaile, and P. G. Kotula, Scr. Mater. **64**, 729 (2011).
[22] N. Argibay, T. A. Furnish, B. L. Boyce, B. G. Clark, and M. Chandross, Scr. Mater. **123**, 26 (2016).
[23] M. Chandross, J. F. Curry, T. F. Babuska, P. Lu, T. A. Furnish, A. B. Kustas, B. L. Nation, W. L. Staats, and N. Argibay, Scr. Mater. **143**, 54 (2018).
[24] A. Argon, *Strengthening Mechanisms in Crystal Plasticity* (Oxford University Press, New York, 2008), Vol. 4.
[25] M. Z. Butt, Philos. Mag. **87**, 3595 (2007).
[26] H. Lim, C. C. Battaile, J. D. Carroll, B. L. Boyce, and C. R. Weinberger, J. Mech. Phys. Solids **74**, 80 (2014).
[27] A. Seeger, J. Zeitsch. Metall. **72**, 369 (1981).
[28] A. Seeger, Mater. Sci. Eng. A **319-321**, 254 (2001).
[29] C. R. Weinberger, B. L. Boyce, and C. C. Battaile, Int. Mater. Rev. **58**, 296 (2013).
[30] G. M. Cheng, W. W. Jian, W. Z. Xu, H. Yuan, P. C. Millett, and Y. T. Zhu, Mater. Res. Lett. **1**, 26 (2013).
[31] Y. Tang, E. M. Bringa, and M. A. Meyers, Mater. Sci. Eng. A **580**, 414 (2013).
[32] M. Chandross and N. Argibay, Phys. Rev. Lett. **124**, 125501 (2020).
[33] R. Ravelo, T. C. Germann, O. Guerrero, Q. An, and B. L. Holian, Phys. Rev. B **88**, 134101 (2013).
[34] S. J. Plimpton, J. Comput. Phys. **117**, 1 (1995).
[35] J. Gruber, H. Lim, F. Abdeljawad, S. Foiles, and G. J. Tucker, Comput. Mater. Sci. **128**, 29 (2017).
[36] P. W. Bridgman, Phys. Rev. **48**, 825 (1935).
[37] J. W. Cahn, Y. Mishin, and A. Suzuki, Acta Mater. **54**, 4953 (2006).
[38] J. Serrin, Z. Angew. Math. Mech. **39**, 295 (1959).
[39] A. Stukowski, Model. Simul. Mater. Sci. Eng. **18**, 015012 (2010).
[40] A. Stukowski, D. Cereceda, T. D. Swinburne, and J. Marian, Int. J. Plast. **65**, 108 (2015).

[41] G. M. Erickson, M. A. Sidebottom, J. F. Curry, D. I. Kay, S. Kuhn-Hendricks, M. A. Norell, W. G. Sawyer, and B. A. Krick, Surf. Topogr. Metrol. Prop. **4**, 024001 (2016).
[42] B. A. Krick, J. R. Vail, B. N. J. Persson, and W. G. Sawyer, Tribol. Lett. **45**, 185 (2012).
[43] C. C. Koch, R. O. Scattergood, K. A. Darling, and J. E. Semones, J. Mater. Sci. **43**, 7264 (2008).
[44] T. Chookajorn, H. A. Murdoch, and C. A. Schuh, Science **337**, 951 (2012).
[45] Z. C. Cordero, B. E. Knight, and C. A. Schuh, Int. Mater. Rev. **61**, 495 (2016).
[46] H. Lim, C. C. Battaile, J. L. Brown, and C. R. Weinberger, Model. Simul. Mater. Sci. Eng. **24**, 055018 (2016).
[47] M. Leitner, W. Schröer, and G. Pottlacher, Int. J. Thermophys. **39**, 1 (2018).
[48] H. Eyring, J. Chem. Phys. **4**, 283 (1936).
[49] See Supplemental Material at http://link.aps.org/supplemental/10.1103/PhysRevMaterials.4.063602 for microscratch data.
[50] L. O. Nyakiti and A. F. Jankowski, Metall. Mater. Trans. A **41**, 838 (2010).
[51] *Standard Test Method for Scratch Hardness of Materials Using a Diamond Stylus* (ASTM International, West Conshohocken, PA, 2017).
[52] T. J. Rupert, J. R. Trelewicz, and C. A. Schuh, J. Mater. Res. **27**, 1285 (2012).
[53] R. J. Asaro and S. Suresh, Acta Mater. **53**, 3369 (2005).
[54] J. Chen, L. Lu, and K. Lu, Scr. Mater. **54**, 1913 (2006).
[55] M. Dao, L. Lu, R. J. Asaro, J. T. M. De Hosson, and E. Ma, Acta Mater. **55**, 4041 (2007).
[56] C. D. Gu, J. S. Lian, Q. Jiang, and W. T. Zheng, J. Phys. D: Appl. Phys. **40**, 7440 (2007).
[57] L. Lu, R. Schwaiger, Z. W. Shan, M. Dao, K. Lu, and S. Suresh, Acta Mater. **53**, 2169 (2005).
[58] M. J. Mayo and W. D. Nix, Acta Metall. **36**, 2183 (1988).
[59] Q. Wei, S. Cheng, K. T. Ramesh, and E. Ma, Mater. Sci. Eng. A **381**, 71 (2004).
[60] Z. J. Wei, Z. L. Wang, H. W. Wang, and L. Cao, J. Mater. Sci. **42**, 7123 (2007).
[61] H. Lim, H. Jong Bong, S. R. Chen, T. M. Rodgers, C. C. Battaile, and J. M. D. Lane, Mater. Sci. Eng. A **730**, 50 (2018).